Satellites unveil easily-fixable super-emissions in one of the world's largest methane hotspot regions

Authors: Itziar Irakulis-Loitxate[1]*, Luis Guanter[1], Joannes D. Maasakkers[2], Daniel Zavala-Araiza[3,4], Ilse Aben[2]

Affiliations:

[1] Research Institute of Water and Environmental Engineering (IIAMA), Universitat Politècnica de València (UPV), 46022, Valencia, Spain.

[2] SRON Netherlands Institute for Space Research, 3584 CA, Utrecht, The Netherlands.

[3] Environmental Defense Fund, Reguliersgracht 79, 1017 LN Amsterdam, The Netherlands.

[4] Institute for Marine and Atmospheric Research Utrecht, Utrecht University, 3584 CC Utrecht, The Netherlands.

* Correspondence to: iiraloi@doctor.upv.es

This paper is a non-peer reviewed preprint submitted to EarthArXiv

Abstract

The reduction of methane emissions from fossil fuel production and use activities has been identified as an essential means for climate change mitigation, but the identification of active emission sources remains elusive for most oil and gas production basins around the world. This limitation can be overcome thanks to recent advances in the detection and quantification of methane point emissions from space. In this work, we combine three complementary satellite data sets to survey single methane emission sources on the west coast of Turkmenistan, one of the largest methane hotspots in the world. We found 29 different emission sources active in the 2017-2020 time period, all of them with emission rates >1700 kg/h and linked to extraction fields mainly dedicated to crude oil production. We estimate that 83% of the identified emitters are inactive flares that directly vent gas to the atmosphere. Several of those emitters showed flaring activity in the past, suggesting a causal relationship between an observed decrease in flaring and the increase in venting. At the regional level, 2020 shows a substantial increase in the number of methane plume detections with respect to previous years. Our results reveal that emissions from the west coast of Turkmenistan could be easily avoided by a proper maintenance of infrastructure and operations, and that new satellite methods promise a revolution in the detection and monitoring of methane point emissions worldwide.

Significance Statement

The detection of methane emissions from fossil fuel production activities around the world is critical for climate change mitigation. We develop and exploit novel satellite methods for an unprecedented large-scale survey of methane point emissions over the West Coast of Turkmenistan. This area is a global hotspot of methane emissions from oil and gas extraction activities. We pinpoint the location of 29 super-emitters, all of them are located in oil fields. We find that a large fraction of emissions is due to gas venting by flares becoming inactive over the last years, which could easily fixed. Our study showcases the upcoming revolution in the use of satellite-based methods to detect, quantify, and monitor point methane emissions.

Introduction

Methane (CH_4) is the second most important anthropogenic greenhouse gas, with a relatively short lifetime in the atmosphere (9±1 years) and with 86 times the global warming potential of carbon dioxide over 20 years (1). During the past few decades, CH_4 concentrations have risen rapidly (2) to record highs that compromise the 2°C temperature target of the Paris Agreement relative to the pre-industrial era (3). Therefore, the reduction of CH4 emissions has been identified as a key climate change mitigation measure in the short to medium term (4).

Among the sectors with the highest contributions to CH_4 emissions is the oil and gas (O&G) industry. CH_4 emissions from this sector are particularly difficult to quantify because they are often the result of unplanned occurrences, i.e. leaks, equipment malfunctions, or abnormal process conditions, of which quantity, duration, and frequency can differ strongly across regions, operators, and stages of the O&G supply chain (5). These events can result in so-called super-emissions, which disproportionately account for a significant fraction of total emissions (6–9). In addition to unforeseen events, emissions from the sector can come from controlled flaring and venting processes, which are, respectively, the combustion and direct liberation of excess natural gas produced. Flaring and venting are primarily done for safety reasons (10), but may also be for economic or operational reasons (11). The objective of flaring is to avoid the direct release of gas in the atmosphere by burning it. However, numerous studies show that the use of flaring does not always guarantee complete combustion of the gas stream in the flare (12–15). Although the use of flaring is preferable to venting from climate perspective, both are seen as indicators of poor resource utilization, where the use of more economically and environmentally sustainable alternatives for the use of excess gas is preferred (16). The use and regulation of flaring and venting depend on the policies and laws in force in each country or region (16, 17), and only a small number of geographic areas have been subject to transparent and publicly verifiable reviews of emissions. Therefore, the credibility of globally reported industrial CH_4 emissions has recently been highly questioned (5). The IEA (International Energy Agency) Methane Tracker report (18) and the U. N. report (4) conclude that a large fraction of the emission mitigation options are technically feasible and cost-effective, and that oil and gas companies can take considerable low-cost and cost-saving measures to reduce CH_4 emissions from pipelines, drilling and other facilities, but this would require greater control of all phases of O&G extraction, processing and transport.

As CH_4 is an odourless and colourless gas for humans, the detection of emissions requires specific sensors sensitive to the gas. Traditionally, the detection and measurement of emissions have been performed through onsite campaigns focusing on locations where suspected undeclared emissions may be present. In situ measurements of ground-based campaigns can be very costly and, depending on their objective, the data collected will be different. For example, an accurate estimate of emission rates is not necessary for leak detection and repair, whereas for the investigation of region-wide emission rates the detection of individual sources might not be required. Airborne campaigns allow coverage of larger areas, but they can be expensive and not very practical in many cases, like in production fields located in remote places (e.g., in the deserts of the Middle East) or for the detection of leaks from long-distance pipelines. In this context, satellites are capable of emission detection and monitoring at different scales (from local to global) and over long periods of time, as opposed to temporally discrete field measurement campaigns. However, detection from space will be limited to large emissions.

Recently, great advances have been made in the detection and quantification of O&G emissions from space. Since 2017, the TROPOMI sensor onboard Sentinel-5P provides daily global CH_4 concentration data with a 7x5.5 km^2 pixel resolution (19). This allows detection of CH_4 concentration enhancements at the regional scale (e.g., 17–21), but in general does not enable the determination of single point sources. On the other hand, the GHGSat instruments and so-called hyperspectral satellite missions like PRISMA, ZY1 AHSI and Gaofen-5 AHSI are able to map CH_4 plumes from single emitters at high spatial resolution (25-50 m GHGSat and 30m the rest) with a detection limit roughly between 100 and 1000 kg/h, suitable to detect medium to strong point emitters worldwide (13, 25, 26). The systematic application of these measurements, however, is limited by their sparse spatio-temporal coverage (see Materials and Methods). The recent realisation of the CH_4 mapping potential of so-called multispectral missions with frequent global coverage holds promise to alleviate this gap (27). Missions like Sentinel-2 (S2) and Landsat 8 (L8) cover the entire world with a relatively high spatial and temporal resolution (20 m and less than 5 days revisit time for S2, and 30 m and less than 15 days revisit time for L8), so they are able to continuously monitor CH_4 plumes under favorable conditions (typically, strong emissions over spatially homogeneous areas). In particular, S2 provides a very high spatio-temporal sampling and data volume, which makes it to be the best mission for systematic monitoring of CH_4 sources in those locations where the site characteristics enable CH_4 retrievals with multispectral missions. L8 and its precursors in the Landsat series do not provide such a high density of observations, but allow to extend the time series to years and even decades before the S2 era. This recently-developed satellite-based CH_4 monitoring scenario allows to detect single point emissions of the largest CH_4 hotspot regions in the world, which are identified with TROPOMI's moderate resolution observations (28).

One example of those CH_4 hotspot regions is the west coast of Turkmenistan, located in the Balkan province on the shores of the Caspian Sea, within the South Caspian Basin (SCB). This is a desert area where the main human activity is the production of O&G and derived products, with a residual presence of other possible anthropogenic CH_4 sources such as livestock, rice fields or landfills (29,

30) and an abundant presence of mud volcanoes (more than twenty), some of which are associated with O&G seepage (31). According to Scarpelli et al. (29), the country of Turkmenistan is one of the largest emitters of CH_4 from O&G-related sources: eighth in oil-derived emissions (0.88 Tg a^{-1}) and ninth in gas emissions (0.52 Tg a^{-1}) in 2016, although the IEA estimates a total of 3.92 Tg a^{-1} of CH_4 emissions in 2020 (almost 3 times more) (18). BP estimates that Turkmenistan has the fourth-largest natural gas reserves in the world with proven reserves of 19.5 trillion cubic meters, nearly 10 percent of the world's total, and is in the top 50 largest oil reserves in the world, with proven reserves of 0.6 thousand million barrels (32). However, its annual production is far below its potential due to the geopolitical situation it maintains (33). Despite this, short-term forecasts indicate that production will increase due to an increase in demand from China in the coming years. Therefore, the country is allocating most of its investments in the energy sector, focusing mainly on the construction of new pipelines, new phases of exploitation in extraction fields, petrochemical plants, and compressor stations (33, 34).

Within the country, CH_4 emissions are not equally distributed. In recent years TROPOMI has detected strong CH_4 concentration enhancements in the western coastal belt belonging to the SCB. In this region there are 26 active fields, 21 onshore and 5 offshore, producing crude oil, condensate, liquefied natural gas (LNG), and gas in different proportions (see Fig. 1). The SCB is also the only basin producing mainly crude oil in Turkmenistan, in contrast to the other basins, the Kushka and Amu-Dar'ya Basins (35, 36), which mainly extract gas.

In this work, we generate a satellite-based high spatial and temporal resolution survey of CH_4 point emissions over the west coast of Turkmenistan based on the hotspot locations provided by the TROPOMI observations. This survey covers an area of approximately 21500 km^2 and the time period between January 2017 and November 2020. Our analysis relies on three different types of space-based CH_4 measurements, which are used synergistically: TROPOMI data facilitate the delimitation of the study area and the identification of the most active regions; the hyperspectral images from PRISMA and ZY1 AHSI allow the identification of medium-to-strong emitters and the accurate quantification of emission rates for those regions in a limited set of days; finally, the multispectral data from S2 and L8 enable the constant monitoring of the emissions from the emission points unveiled by the hyperspectral data (see Materials and Methods). We choose the west coast of Turkmenistan for this study because it offers an ideal combination of extreme CH_4 emissions with a bright and relatively homogeneous surface. This allows us to best evaluate this unprecedented combination of CH_4 data streams as well as to extract its full potential.

Results

Analysis of emission sources

Combining the hyperspectral and multispectral high spatial resolution satellite data, we have detected 29 emission points with activity between January 2017 and November 2020 (Fig. 2). The areas with the highest density of point sources in our high-resolution survey coincide with the strongest CH_4 enhancements over the west coast of Turkmenistan, as seen in the regional-scale maps generated from TROPOMI moderate resolution data (Fig. 1)

The 20-30 m sampling of the hyperspectral and multispectral satellites in combination with very high-resolution imagery from Google Earth, Bing Maps and Esri (<2.5m/pix) provide sufficient information to determine the coordinates of emission sources with high precision, especially for those emitters with many detected plumes (see Materials and Methods). Combining these data, we have identified the sources of 26 of the 29 points. We find that the vast majority of the emitters (24 of them) are inactive flares that vent gas. Several of them have flaring activity before 2017 according to the historical record of the S2, Landsat 5, 7, and 8 satellites, and Google Earth, Bing and Esri images, and three of them had an active flare at the beginning of the study period (Fig.

S1), followed by CH_4 emissions as soon as the flare disappeared. The flaring activity is discussed in more detail in the following sections.

The 24 emitting flares are distributed across different onshore fields of the SCB with a higher density in the Goturdepe, Barsa-Gelmez and Korpeje fields (Fig. S2). These three fields have the highest production (Table 1) and are also three of the oldest ones in the basin. This coincides with the 2013 Carbon Limits report, which indicates that most of the flares are concentrated in fields built before 1990 (37). Most of the emitters are in fields where the predominant activity is crude oil and condensate production, except for the Korpeje field that extracts mainly gas (see Table 1). Two of the emitting flares are in an oil power plant linked to the Goturdepepe field. The fields where we have detected emissions are directly managed by two large state companies, which at the same time control most of the Turkmenistan fields (35). Although all SCB fields have been analyzed, no emissions have been recorded from the fields managed by the other five companies operating in the area, which are based in other countries.

Regarding the two other emitters with a known origin, the plumes from points A.10 and E.2 (see Fig. 2) are due to pipeline leaks that persist over several months. In the case of A.10, the leak is active for more than a year between 2019 and 2020, while at E.2, we observe emissions from April to October 2018. It has been possible to confirm that these two emissions are due to leaks because the start of the emission coincides with anomalies in the surface (visible in RGB images), and the CH_4 plumes seem to originate in pipelines. In E.2, it is also possible to see a liquid spill emanating from the leak (see Fig. S3).

In the case of the three remaining emission points (A.8, A.9 and B.1), it is difficult to attribute them to a particular source. Leaks are the most likely origin, given that the three points are located just above pipes, that the facilities are old in these fields and that, according to the 2013 Carbon Limits report, the pipeline network (controlled by the national gas company Turkmengas) "is characterised by its old and inefficient equipment" (37). However, we do not have access to records of incidents or leaks recorded by the operators and cannot confirm the source of the emissions because the very high-resolution imagery available is not sufficiently up to date to support this hypothesis, and the resolution of S2 and Landsat imagery is not sufficient in these cases to distinguish a clear change in the surface in visual imagery. Regarding the temporal evolution of these emissions, Point A.9 only shows emissions during September 2020, which would indicate either that the emission source has already been fixed or that the emission rates have decreased below the S2 detection limit. Point A.8 shows emissions since 2017, whereas point B.1 has been emitting at least since 2015, according to L8 detections. Both have maintained emissions at least until the end of our study period in December 2020.

None of the detected emitters are linked to mud volcanoes despite those being potential sources of CH_4 and having a high presence in the area.

Magnitude of the emissions

We have developed methods to quantify CH_4 concentration enhancements and flux rates from the hyperspectral data (13). Using the hyperspectral data, we have detected 25 plumes from 12 of the emitters on different dates (see Materials and Methods). The estimated emission fluxes vary considerably, with 1.400 ± 400 kg/h being the lowest emission and 19.600 ± 8.000 kg/h the largest detected emission (see Fig. S4).

The coincident overpass time of S2, PRISMA and ZY1 (2 - 5 minutes difference) has enabled us to capture emissions concurrently with S2 and the hyperspectral systems (see Fig. S5). Using the accurate CH_4 concentration enhancement maps from the hyperspectral systems as a reference, we can assess the detection limits of the substantially lower signal-to-noise ratio S2 observations. This exercise shows that S2 can detect emissions of at least 1800 ± 200 kg/h for the Turkmenistan desert scenes, as this is the smallest emission for which we have a coincident detection with the hyperspectral data. This is the minimum flux rate that we set for the plumes detected by S2 (944 plumes in total) between January 2017 and November 2020 (Fig. S4).

We have estimated the approximate annual flux emitted from the 29 emitters identified in the study area, i.e., the total CH_4 flux emitted from the sources that we sample in our study. This calculation is based on an average flux rate estimated from the 25 plumes detected with the hyperspectral data and the average emission frequency calculated from the multispectral data set. Further details of the annual calculation are given in Materials and Methods. As a result, we have obtained a resulting integrated flux of 0.28 Tg a^{-1} (0.25-0.31 Tg a^{-1} 95% confidence interval).

Temporal evolution of the emissions

The monitoring of emissions during 2017-2020 using S2 data has shown a remarkable difference in the number of detected plumes from each emitter over time. In general, 2018 was the year with the fewest detected emissions, while 2020 has been the year with the most detected emission plumes, double the number detected in 2018 (see Fig. 4 and Table 1). This relationship also holds when we normalize the number of emissions by the number of clear-sky observations in each period.

Not all fields have had the same evolution. Figure 4 shows the examples of the Goturdepe, Korpeje and Gogerendag fields (labelled with emitters A.X, D.X and C.X, respectively) as representative cases of different temporal evolution patterns. Goturdepe is one of the fields with the highest number of identified emitters, and its temporal evolution clearly shows a decrease in the number of emissions between 2018 and the beginning of 2019, while in the years 2017 and 2020, the emission density is notably higher. Regarding the Korpeje field, Varon et al. reported in 2019 emissions from three different points (38), one of which is named in this paper as D.7. Immediately after the article submission (May 2019) emissions stopped from that source, but both our analysis and the one by Varon et al. (2021) (27) show that emissions resumed after a few months (according to our observations in September 2019). Finally, the Gogerendag field stands out for the direct relationship between the end of the use of flaring and the start of emissions, i.e., at the beginning of the monitoring period, emitters in this field had flaring activity, but CH_4 emission events began to occur right after the flaring signal was no longer visible. In the second half of 2019 it can be seen how after several months of flaring inactivity, both emitters released CH_4 on the same day, and then a flare is observed intermittently at C.1 before it remains off at least until the end of our study period. Once flaring was inactive, the number of CH_4 emissions detected by S2 increased. This same flaring-emission relationship is repeated at point F.3, which shows an intense flaring signal at the beginning of the study, but in July 2018, the flaring disappears. In July 2019, CH_4 emissions start to be observed intermittently until the end of the study period.

Analysing the emitters individually, we also see that there is wide variability in their emitting frequency. Of the 29 points, 6 show emissions on only between 1 and 3% of the observed clear-sky days, i.e., they rarely present emissions above our 1700 kg/h detection limit. On the opposite side, 5 points show emissions in more than 38% of the observed days. For example, Figure 3 shows a S2 detection series from A.3 (29% emission frequency) whose emissions persist during the entire 2017-2020 period. The low frequencies imply that we have detected large CH_4 emissions between 1 and 7 times during the whole observation period, these emissions could be explained by emergencies or well purging, that are very unusual events, and where the law allows the venting of large amounts of gas from flaring systems for a short period. However, the more frequent emitters would conflict with the "Rules for the Development of Hydrocarbon Fields" of the Turkmen law, which bans continuous gas flaring and venting (37). Detailed information on the frequency of emissions is provided in Table S1 and Figure 2.

We also look at the emissions of the region before our 2017-2020 core study period. First, the longer time series of L8 satellite data reveal that at least 15 of the 29 emitters identified in the study period were already emitting large amounts of CH_4 before January 2017, as shown in Figure 3 (first window, right-hand side panel). Second, the SCIAMACHY sensor onboard ENVISAT (39) also provides information on the history of emissions in the area, in this case, at the regional scale. Comparing the distribution of our single detections with the regional XCH_4 map from TROPOMI (Figs. 1-2), we can infer that the CH_4 enhancement observed by TROPOMI in the northern part of the study area is the result of many moderate to high-frequency emitters, while in the south the areas of CH_4 enhancement are related to one or a few very high-frequency emitters (Fig. S6). This relationship holds in older data from SCIAMACHY. Between 2003-2010 SCIAMACHY already observed a higher CH_4 concentration in the northern area of the SCB, over the Goturdepe and Barsa-Gelmez fields (emitters A.X and B.X) and another hot spot over the Korpeje (D.X) and Gamyshlja Gunorta (E.X) fields but did not observe a CH_4 enhancement over the southernmost Keymir (F.X) and Akpatlavuk (G.X) fields. If we look at the year of installation of the facility, we find that most of the emitters in the first four fields already existed before 2010, but emitter F.1, which is the one with the highest frequency in Keymir, was built just in 2010, according to Landsat images, and emitter G.1, the only one in Akpatlavuk, was built in 2015. So, these two points did not contribute to the average result of the data collected by SCIAMACHY (Fig. S6). Likely, other emitters were also active in the observation period of SCIAMACHY, although they might not have emitted gas during the entire period. On the other hand, emitters F.1 and G.1 did not exist during that time, and thus their emissions are only reflected in the TROPOMI data set. These data also demonstrate that this type of emission has been occurring for many years and that the origin of these long-term CH_4 enhancements is in the venting of gas, mainly from oil and condensate fields.

Flaring

According to VIIRS data, flaring has been progressively decreasing over the SCB since 2016. For example, the flare volume in 2019 was about 40% lower than in 2012 (Fig. S7). This trend is the same if we look at the state-level data, where the flare volume has continuously decreased since VIIRS records have been kept, and in 2019 it is almost half of what it was in 2012 (2.42 billion cubic meters in 2012 and 1.34 billion cubic meters in 2019) (40).

As we previously discussed, several of the CH_4 emitters detected in our survey follow this trend of flaring reduction. In particular, C.1, C.2 and F.3 have flaring activity at the beginning of the monitoring but then change from flaring to gas emission. In addition, we have observed that at least six other emitters had an active flame in the past, but vented gas later (Fig. S1). The fact that several of the emitters currently venting CH_4 showed flaring activity in the past suggests a relationship between the decrease in flaring at the expense of an increase of venting.

The effect of the use of flaring can also be noticed in the TROPOMI data where, for example, we see the influence of point E.1 (high-frequency emitter of the Gamyshlja-Gunorta field). This emitter kept showing flaring activity until 2005 while it is emitting CH_4 during the TROPOMI monitoring period. On the other hand, we hardly see the influence of the two Gogerendag emitters (C.1 and C.2), which kept the flare active until 2019, and their emissions are still not noticeable in the TROPOMI data (Fig. S6).

Discussion

In this study, we have used a combination of satellites to produce a large-scale survey of individual CH4 emitters active between 2017 and 2020 on the west coast of Turkmenistan, one of the world's largest CH4 hotspot regions as shown by TROPOMI observations. First, areas of interest within the region have been identified using medium-resolution data from TROPOMI. Two types of high-resolution data (multi- and hyperspectral) have then been used to detect, quantify, and monitor the activity of the identified 29 strong CH4 emitters over time. In particular, hyperspectral satellites have mapped plumes with fluxes between 1.400 ± 400 kg/h and 19.600 ± 8.100 kg/h, which indicates that the emissions from Turkmenistan are often extremely high; the S2 multispectral satellite has enabled the systematic monitoring of emissions above 1700 kg/h, showing an increase in the number of detections in 2020 compared to the previous years, and the longer time series of the L8 mission (2013-today) has shown that several emitters have been venting CH4 beyond the S2 observation period.

The main results of this study reveal that the large amounts of CH_4 emitted in this region are mainly due to the venting of gas from oil fields. We find that venting is related to the decrease in the use of flaring as a method to treat excess gas. Secondly, the emissions not related to venting are linked to the bad condition of the installations, concretely of the pipelines, which have gas leaks during long time periods. These emissions could be easily and rapidly fixed: in the case of inactive flares it would be sufficient to activate the flares, although other more sustainable methods as gas capture would be preferable (41); in the case of pipeline leaks, it is necessary to improve maintenance and surveillance. Identifying these high emitting sources is fundamental for any mitigation strategy, as their elimination would result in an important reduction of CH_4 emissions. In particular, we estimate that the emissions identified in this study amount to 0.28 Tg a^{-1} (0.25-0.31 Tg a^{-1} 95% confidence interval), which could be easily avoided. It is unknown how these numbers would scale to the global scale, but we can already speculate that a massive amount of CH_4 emissions could indeed be avoided if greater control actions were taken on oil and gas extraction operations.

The 29 emitting sources found in the study only represent emitters above the detection limit of the satellites used in this work. In these cases, synergy with a regional mapper (and inverse modelling) such as TROPOMI or the upcoming MethanSAT missions could provide the full picture of emissions for the basin. In addition, rapid source identification and data interpretation can provide valuable clues to understand the problem in each case, and thus select appropriate methods for effective mitigation of smaller emissions.

High-resolution satellites capable of detecting CH4 emissions, in combination with mid-resolution satellites with daily global coverage such as TROPOMI and its successor Sentinel-5 instruments, bring a new era in the monitoring of industrial emissions, both locally and globally, with the potential to provide early warnings in near real-time. In addition to the already operational high-resolution satellites (GHGSat, PRISMA, ZY1, S2 and Landsat), new missions such as MethaneSAT, EMIT, Carbon Mapper, EnMAP, CHIME or SBG are expected to reinforce possible monitoring systems even further.

Our results also point at the risks of penalizing flaring without effective measures to control venting. The possibility of flaring cessation at the expense of venting is a problem that has been discussed in the past (41) since monitoring flaring is easy to carry out by satellites, but venting was easy to hide until now. Furthermore, the methods we use here can also be applied to track progress of flare reduction strategies in other areas of the world.

Materials and Methods

Definition of the study area with TROPOMI XCH_4 data

The TROPOspheric Monitoring Instrument (TROPOMI) sensor onboard ESA's Sentinel-5P satellite (19) provides daily global coverage of CH_4 data with 7 km x 7 km (since August 2019 5.5 km x 7 km) pixel resolution in nadir that allows finding areas with high CH_4 concentration enhancements. The approximate location of the strongest sources in the study area has been identified using the wind rotation method introduced by Maasakkers et al. (2021) (28). After identification of an area with large CH_4 concentrations, data from individual days is rotated around a possible target point using the wind direction at the location. In this manner, the scenes are rotated so that the wind vector is always pointing northward, these rotated scenes are then averaged. By doing this exercises for a full grid of points, the location can be determined where the mean downwind concentrations are most significantly enhanced compared to the mean upwind concentrations, resulting in the most likely location of the source (28). TROPOMI pinpointing identified five key points (see Fig. S8) where we started the search for point sources of emission. In addition, the Korpeje area was already known for its strong and frequent point source emissions (25).

High-resolution Hyperspectral & Multispectral data

This study has used both hyperspectral and multispectral satellites, which are complementary for the detection and monitoring of CH_4 emissions. Hyperspectral instruments offer a relatively high sensitivity to CH_4 thanks to tens of spectral channels located around the strong CH_4 absorption feature around 2300 nm, but acquisitions are made upon request and their coverage is sparse in space and time. In turn, multispectral systems provide frequent and spatially-continuous observations over any region on Earth, but with a very limited sensitivity to CH_4.

Use of hyperspectral data for CH_4 detection and quantification

For this study, we have collected data from the ZY1 AHSI and PRISMA missions, which are the only two hyperspectral satellite missions sampling the 2300 nm spectral region and with an open data policy. The Chinese ZY1 mission was launched in September 2019 and has onboard the AHSI sensor whose images cover a 60X60 km^2 area, while the Italian PRISMA mission, launched in March 2019, provides images with 30X30 km^2 coverage. Both missions have a spatial resolution of 30 m.

All hyperspectral data acquisitions took place during 2020 (the last year covered by this study). Acquisition requests were first made with focus on the key points identified by TROPOMI, and then those were extended to other possible key areas (see the following subsection). Due to the difficulty to obtain data from these sensors in the short term, we could not cover some areas in that time range. Many PRISMA images have been acquired from the catalogue, while others have been obtained based on requests for targeted locations. In total, we have obtained 12 images from PRISMA and one from ZY1 (see Fig. S9).

The hyperspectral images have allowed us to observe CH_4 emissions with 30m spatial resolution and quantify the emissions using the matched filter method (13). The quantification has been done with the integrated methane enhancement (IME) method (42), and we have used 1-h average 10-m wind ($U10$) data from the NASA Goddard Earth Observing System-Fast Processing (GEOS-FP) meteorological reanalysis product at 0.25°× 0.3125° resolution (43) to get the Flux Rates (Q). The details of our processing of hyperspectral data are provided in Guanter et al. (2021) (44).

Use of multispectral data for CH_4 monitoring

For the temporal monitoring of emissions, we have used the Sentinel-2 Level 2A (L2A) product from both S2-A and B satellites of ESA's Copernicus program, whose data are openly available on the Copernicus Open Access Hub official portal.

The S2 CH_4 detection limit and the estimation of the emissions detected in S2 monitoring has been defined using the quantified plumes coincident with S2 detections, as the three satellites have approximately the same overpass time with a few minutes difference (between 2 and 5) in the observations used. We have identified nine simultaneous plumes indicating that the detection limit of S2 is close to 1700 kg/h (see Fig. S5). This relationship holds if the plume maintains concentrations above ~3800 ppm m. For example, in cases where the wind speed is very high, and the emitted gas disperses rapidly, the plume tail disappears, and the pixels in the plume have lower concentrations despite being associated with a high emission flux. There are several examples of this in Figure S4, where hyperspectral sensors detect plumes on 2020-07-31 and 2020-09-11 that S2 missed, i.e., S2 has not detected emissions with fluxes lower than 1700 kg/h that PRISMA and ZY1 have with a few minutes difference. This detection limit value is slightly lower than Varon et al.

(2021) (27) indicated (~3000 kg/h) for the most optimal surfaces, as is the case in most of Turkmenistan.

The detection of single plumes from S2 data is often challenging because of its relatively low sensitivity to CH_4 concentration enhancements. We have a priori predetermined areas with potential emitters on which to focus the search of possible plumes. These are: the area near the TROPOMI pinpoints (see Fig. S8), emission points detected in the ZY1 and PRISMA hyperspectral images (see Fig. S4), O&G extraction fields in the SCB according to (35, 36), pipeline crossings, flares that in the past had shown an active flame, and mud volcanoes.

To detect CH_4 emissions with S2, we have selected bands B11 and B12, with 20 m pixel resolution. The B11 band extends over a set of weak CH_4 absorption lines near 1650 nm, and the B12 band includes stronger absorption lines in the 2200-2300 nm range so that the average optical depth of CH_4 in B12 is five times that of B11 (27). The identification of emissions has been carried out using a dynamic multitemporal method, where we consider all observed days by both the S2 A and B satellites. We have applied the B12/B11 band ratio to the clear-sky days and, using the timelapse tool provided in the online service EO Browser of Sentinel Hub (45), we have obtained the continuous record of the time series of the study area (<3 km^2 in each timelapse). We have discarded cloudy images with an automatic filter available in the EO Browser service and manually sandstorm days that do not allow a clear view of the surface.

The S2 detection figures shown in this paper (Fig. 3 and Fig. S5) have been obtained applying the B12 and B11 bands ratio of two contiguous days from the same satellite, i.e., the equation described below but always ensuring that the detection is taken by the same satellite, S2A or S2B, on both days.

$$R = \frac{B12/B12'}{B11/B11'}$$

where R is the result of the band ratio $B12$ and $B11$ are the bands of the emission day, and $B12'$ and $B11'$ are the bands of the nearest clear-sky day observed with the same S2A or S2B satellite on which there is no emission. We use detections from the same satellite on both days because there is a wavelength offset in the B11 and B12 bands between 1.8 and 21.7 nm from S2A to S2B (46), so the combination would increase the noise and make the result less clear. This method provides the CH_4 plume avoiding the maximum interference in the signal from other surface components.

The simple B12/B11 band ratios provide an image where CH_4 pixels take low values (<0.9) which contrast with the rest of the surface that is close to 1. The result would be similar to the one proposed by Varon et al. (2021) (27) in the Multi-Band/Single-Pass (MBSP) method, but in this case, without normalising the band ratio and dynamically comparing the emission days with the adjacent days. The comparison of each image with the days immediately adjacent to it using the timelapse allows enhancing the CH_4 signal by minimizing the effect of surface variability since the CH_4 plumes change shape depending on the activity, emission intensity of each day, and the wind direction that normally changes from one day to another. This dynamic method has proven to be the most effective to identify the weakest emissions, which, analysed individually, would go unnoticed, and to lower the detection limit of S2 to about 1700 kg/h on the most optimal surfaces. The 20m pixel resolution of S2 and multiple observations of plumes from the same source have provided sufficient accuracy to identify the emission source.

We have obtained the L8 results in the same way as S2, but in this case with the B06 and B07 bands, where B06 extends over the weak CH_4 absorption lines between 1570-1670nm, and B07 covers strong absorption lines in the range 2110-2290nm with a 30m resolution. In the case of L8, the overpass time is about 20 minutes different from ZY1, PRISMA and S2, so that coincident detections on the same day have not been considered valid for empirical comparison. L8 has a revisit cycle of 16 days. We have used data from the entire L8 time series (2013-today).

Annual quantification

We have estimated an integrated annual emission rate (Q_a) from all 29 sources detected in this study. For this estimation, we rely on the Q values estimated for the single plumes obtained from the hyperspectral data (Fig. S4) in order to obtain an average hourly flux rate ($\bar{Q}$)characterizing the emissions in the area. This average flux rate is scaled in time using an average emission frequency number ($\bar{f}$) which is obtained from the S2 plume detections (O. E. % in Table S1). The total annual emission rate is then given by:

$$Q_a = 24 \cdot 365 \cdot N \cdot \overline{Q} \cdot \overline{f}$$

where *N* is the number of emitters, i.e., 29 emission sources.

This estimate is based on statistics from emission intensity and frequency data sampling the four years of monitoringcovered in this study. The resulting annual flux only represents the annual emission flux from large emitters, and underestimates the real one, as only emissions above the S2 detection limit are considered in the calculation of the average emission frequency. As a result, we have obtained an annual estimate of 0.28 Tg of CH_4 emitted per year, with a 95% confidence interval between 0.25 and 0.31 Tg a^{-1}.

The 95% confidence interval was obtained by non-parametric bootstrapping of all the results obtained from combining the Q of each of the 25 plumes with the emission frequencies (f) of each of the 29 identified emitters.

Emitter identification

The identification of the sources was carried out by inspection of high-resolution visual images from Google Earth, Bing Maps and Esri, depending on the acquisition date available for each area on each platform.
In the initial approach of the study, we also considered mud volcanoes as possible sources of CH_4 emission. However, after observing the different potential areas, it has not been possible to link any of the observed plumes to a mud volcano.
In three cases, we were not able to identify the origin of the emissions due to lack of up-to-date very high-resolution surface imagery (in some southern areas most recent image is from 2015 and Planet's 3m/pix images are not enough for these cases) and insufficient geographic information about Turkmenistan's O&G infrastructure.
Regarding the emitters identified as flares, there is a wide variety of flare systems within the O&G sector of which characteristics depend on multiple factors such as calorific power of the burning fuel, physical state (gas, liquid, or mixture), pressure, flow, geographic location for the population or other activities, availability of land for the installations, economic availability, ... In general, we can distinguish two main groups of flares: elevated flares that are mainly used in the burning of gaseous waste in plant emergencies (due to power failures, composition, and fires) and are more oriented to sudden alterations, and ground flares that are generally used for moderate or continuous flow. Linked to the second, we can distinguish a third group, the pit flares, which usually burn liquid or gaseous waste in unpopulated areas to meet environmental standards.
In Turkmenistan, we have detected emissions from all three types of flares. Throughout the study, they have all been referred to as the same "flare" emitter type, although in Table S1, there is a more precise classification separating them into the three groups.

The identification of the emitters, mainly flares, has been verified by the Carbon Limits group, which has experience in field measurements in Turkmenistan.

Flaring signal

Flaring can be detected by satellites with bands in the SWIR, due to the flame's strong signal in that spectral region, with the emission peak at 1.6 µm (47).

In the 2017-2020 period, three of the emission points have shown an intense signal in the B12 band of S2 coming from flaring, i.e., those days the excess gas was burning instead of venting it directly to the atmosphere. These three points maintained a constant signal for several months until the flaring signal disappeared, and we started detecting CH_4 emissions (see Fig. 4 Gogerendag case). S2 data are only available as of January 2017, so to check if there had been any faring signal in the past for the rest of the emitters, we have observed with Landsat 8, 7 and 5 data (up to 1984) (48), using the Google Earth Engine platform, the historical VIIRS signal (up to 2012) using SkyTruth's flaring maps (40, 49), and FIRMS for MODIS (up to 2000) and additional information from VIIRS. We have also used historical high-resolution Google, Bing and Esri imagery to check if flaring was also used in the past, as the powerful flaring flames can also be seen in the visible (see Fig. S1).

Acknowledgments

The authors thank the team that realized the TROPOMI instrument and its data products, consisting of the partnership between Airbus Defense and Space Netherlands, KNMI, SRON, and TNO, commissioned by NSO and ESA. Sentinel-5 Precursor is part of the EU Copernicus program, Copernicus (modified) Sentinel-5P data (2018-2020) have been used. We thank the Sentinel Hub service for providing the EO Browser service, which was key to the development of the study. Thanks to the Environmental Defense Fund (EDF) for providing data about the O&G fields of the study area, and the Carbon Limits group for contributing to the verification of the emission sources. We thank the Italian Space Agency for the PRISMA data used in this work. Dr. Yongguang Zhang from University of Nanjing is also thanked for his support to get access to ZY1 AHSI data, and Dr. Javier Gorroño from Universitat Politècnica de València for his assistance in the uncertainty estimations.

References

1. M. Etminan, G. Myhre, E. J. Highwood, K. P. Shine, Radiative forcing of carbon dioxide, methane, and nitrous oxide: A significant revision of the methane radiative forcing. *Geophys. Res. Lett.* (2016) https:/doi.org/10.1002/2016GL071930.
2. M. Saunois, *et al.*, The global methane budget 2000-2017. *Earth Syst. Sci. Data* (2020) https:/doi.org/10.5194/essd-12-1561-2020.
3. E. G. Nisbet, *et al.*, Very Strong Atmospheric Methane Growth in the 4 Years 2014–2017: Implications for the Paris Agreement. *Global Biogeochem. Cycles* **33**, 318–342 (2019).
4. United Nations Environment Programme and Climate and Clean Air Coalition, “Global Methane Assessment: Benefits and Costs of Mitigating Methane Emissions” (2021).
5. U. N. E. P. (UNEP), Oil and Gas Methane Partnership (OGMP) 2.0 Framework **|** Climate & Clean Air Coalition. 1–18 (2020).
6. R. A. Alvarez, *et al.*, Assessment of methane emissions from the U.S. oil and gas supply chain. *Science (80-.).* **361**, 186–188 (2018).
7. D. Zavala-Araiza, *et al.*, Super-emitters in natural gas infrastructure are caused by abnormal process conditions. *Nat. Commun.* **8**, 1–10 (2017).
8. A. R. Brandt, G. A. Heath, D. Cooley, Methane Leaks from Natural Gas Systems Follow Extreme Distributions. *Environ. Sci. Technol.* **50**, 12512–12520 (2016).
9. T. Lauvaux, *et al.*, Global Assessment of Oil and Gas Methane Ultra-Emitters. arXiv [Preprint] (2021) https://doi.org/10.31223/X5NS54 (May 19, 2021).
10. O. S. Ismail, G. E. Umukoro, Global Impact of Gas Flaring. *Energy Power Eng.* **04**, 290–302 (2012).
11. U.S. Department of Energy. Office of Oil and Natural Gas, Natural Gas Flaring and Venting : State and Federal Regulatory Overview , Trends , and Impacts. *U.S. Dep. Energy*, 72 (2019).
12. D. R. Lyon, *et al.*, Aerial Surveys of Elevated Hydrocarbon Emissions from Oil and Gas Production Sites. *Environ. Sci. Technol.* (2016) https:/doi.org/10.1021/acs.est.6b00705.
13. I. Irakulis-Loitxate, *et al.*, Satellite-based Survey of Extreme Methane Emissions in the Permian Basin. *Sci. Adv.* (2021).
14. A. Gvakharia, *et al.*, Methane, Black Carbon, and Ethane Emissions from Natural Gas Flares in the Bakken Shale, North Dakota. *Environ. Sci. Technol.* **51**, 5317–5325 (2017).
15. D. Zavala-Araiza, *et al.*, A tale of two regions: methane emissions from oil and gas production in offshore/onshore Mexico A tale of two regions: methane emissions from oil and gas production in offshore/onshore Mexico. *Environ. Res. Lett* **16**, 24019 (2021).
16. World Bank Group, Global Gas Flaring Reduction A Public-Private Partnership World Bank Group A VOLUNTARY STANDARD FOR GLOBAL GAS FLARING AND VENTING REDUCTION (2004).
17. EUROPEAN COMMISSION, “COMMUNICATION FROM THE COMMISSION TO THE EUROPEAN PARLIAMENT, THE COUNCIL, THE EUROPEAN ECONOMIC AND SOCIAL COMMITTEE AND THE COMMITTEE OF THE REGIONS on an EU strategy to reduce methane emissions” (2020) (April 14, 2021).
18. IEA, “Methane Tracker 2020” (2020) (May 19, 2021).
19. J. P. Veefkind, *et al.*, TROPOMI on the ESA Sentinel-5 Precursor: A GMES mission for global observations of the atmospheric composition for climate, air quality and ozone layer applications. *Remote Sens. Environ.* **120**, 70–83 (2012).
20. D. H. Cusworth, *et al.*, Detecting high-emitting methane sources in oil/gas fields using satellite observations. *Atmos. Chem. Phys.* **18**, 16885–16896 (2018).
21. Y. Zhang, *et al.*, Quantifying methane emissions from the largest oil-producing basin in the United States from space. *Sci. Adv.* **6**, eaaz5120 (2020).
22. O. Schneising, *et al.*, Remote sensing of methane leakage from natural gas and petroleum systems revisited. *Atmos. Chem. Phys.* **20**, 9169–9182 (2020).
23. J. Barré, *et al.*, Systematic detection of local CH 4 anomalies by combining satellite measurements with high-resolution forecasts. *Atmos. Chem. Phys* **21**, 5117–5136 (2021).

24. J. A. de Gouw, *et al.*, Daily Satellite Observations of Methane from Oil and Gas Production Regions in the United States. *Sci. Rep.* **10** (2020).
25. D. J. Varon, *et al.*, Satellite Discovery of Anomalously Large Methane Point Sources From Oil/Gas Production. *Geophys. Res. Lett.* **46**, 13507–13516 (2019).
26. D. H. Cusworth, *et al.*, Multisatellite Imaging of a Gas Well Blowout Enables Quantification of Total Methane Emissions. *Geophys. Res. Lett.* **48** (2021).
27. D. J. Varon, *et al.*, High-frequency monitoring of anomalous methane point sources with multispectral Sentinel-2 satellite observations. *Atmos. Meas. Tech.* **14**, 2771–2785 (2021).
28. J. D. Maasakkers, et al., Space-based identification and quantification of methane emissions from landfills [in preparation] (2021).
29. T. Scarpelli, *et al.*, A global gridded (0.1° × 0.1°) inventory of methane emissions from oil, gas, and coal exploitation based on national reports to the United Nations Framework Convention on Climate Change. *Earth Syst. Sci. Data Discuss.*, 1–21 (2019).
30. European Commission Joint Research Centre (EC-JRC), Environmental Assessment Agency (PBL), Emissions Database for Global Atmospheric Research (EDGAR), release EDGAR v5.0 (1970 - 2015) of November 2019. *Crippa, M., Oreggioni, G., Guizzardi, D., Muntean, M., Schaaf, E., Lo Vullo, E., Solazzo, E., Monforti-Ferrario, F., Olivier, J.G.J., Vignati, E., Foss. CO2 GHG Emiss. all world Ctries. - 2019 Report, EUR 29849 EN, Publ. Off.* (2019).
31. D. Oppo, R. Capozzi, A. Nigarov, P. Esenov, Mud volcanism and fluid geochemistry in the Cheleken peninsula, western Turkmenistan. *Mar. Pet. Geol.* **57**, 122–134 (2014).
32. BP, Statistical Review of World Energy, 2020 | 69th Edition. *Bp* **69** (2020).
33. S. Pirani, *Central Asian Gas: prospects for the 2020* (2019).
34. *Sustainable Infrastructure for Low-Carbon Development in Central Asia and the Caucasus* (OECD, 2019) https:/doi.org/10.1787/d1aa6ae9-en (March 4, 2021).
35. Rystad Energy - Your Energy Knowledge House (April 18, 2021).
36. K. Rose, *et al.*, “Development of an Open Global Oil and Gas Infrastructure Inventory and Geodatabase” (2018) https:/doi.org/10.18141/1427573.
37. Torleif Haugland, *et al.*, “Associated petroleum gas flaring study for Russia, Kazakhstan, Turkmenistan, and Azerbaijan” (2013).
38. D. Varon, *et al.*, High-frequency monitoring of anomalous methane point sources with multispectral Sentinel-2 satellite observations. *Atmos. Meas. Tech. Discuss.*, 1–21 (2020).
39. C. Frankenberg, *et al.*, Global column-averaged methane mixing ratios from 2003 to 2009 as derived from SCIAMACHY: Trends and variability. *J. Geophys. Res.* **116**, D04302 (2011).
40. SkyTruth | Flaring Volume Estimates (March 5, 2021).
41. R. Calel, P. Mahdavi, The unintended consequences of antiflaring policies—and measures for mitigation. *Proc. Natl. Acad. Sci. U. S. A.* **117**, 12503–12507 (2020).
42. C. Frankenberg, *et al.*, Airborne methane remote measurements reveal heavy-tail flux distribution in Four Corners region https:/doi.org/10.1073/pnas.1605617113 (August 27, 2020).
43. A. Molod, *et al.*, The GEOS-5 Atmospheric General Circulation Model: Mean Climate and Development from MERRA to Fortuna. *NASA TM-2012-104606* (2012).
44. L. Guanter, *et al.*, Mapping methane point emissions with the PRISMA spaceborne imaging spectrometer. arXiv [Preprint] (2021). https://doi.org/10.31223/X5VC9C (May 19, 2021)
45. Sentinel Hub (May 18, 2021).
46. MSI Instrument – Sentinel-2 MSI Technical Guide – Sentinel Online - Sentinel (April 19, 2021).
47. C. D. Elvidge, M. Zhizhin, K. Baugh, F. C. Hsu, T. Ghosh, Methods for global survey of natural gas flaring from visible infrared imaging radiometer suite data. *Energies* **9** (2016).
48. M. A. Wulder, *et al.*, Current status of Landsat program, science, and applications. *Remote Sens. Environ.* **225**, 127–147 (2019).
49. SkyTruth Flaring Map (March 5, 2021).

Figures and Tables

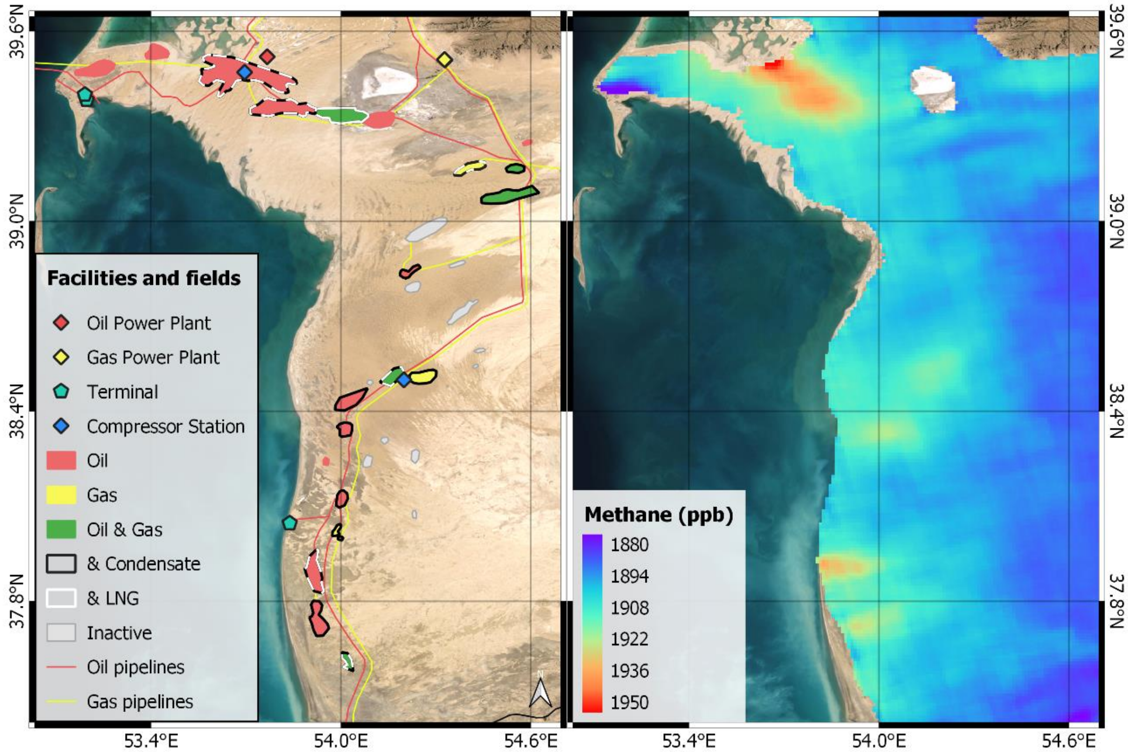

Figure 1. Representation of the study area. Left, oil and gas fields classified according to the type of production activity based on Rystad database (35): oil, gas, condensate, liquefied natural gas (LNG), and the combination of several of them; the location of processing plants, terminals, compressor stations and pipelines along the South Caspian Basin as provided in (36) are also depicted. Right, 0.1º composite of CH_4 concentration in the atmospheric column from TROPOMI data between November 2018 and November 2020. Background satellite image from ESRI.

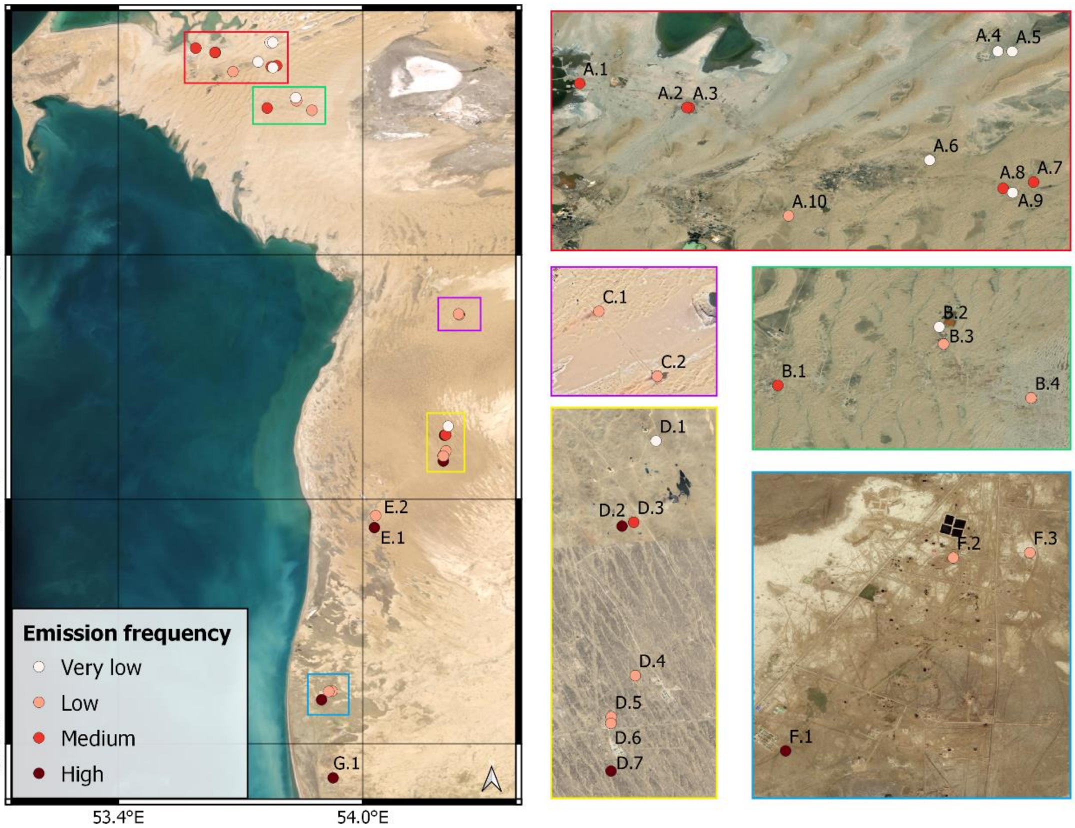

Figure 2. Spatial distribution of point emissions in Turkmenistan's South Caspian Basin. The emission frequency corresponds to the number of emissions detected by S2 with respect to the number of clear-sky days with S2 overpasses between 2017 and 2020, where "high" represents an emission frequency range between 48 - 37 %, "medium" 37 - 15 %, "low" 15 - 3 %, and "very low" 3 - 1 %. Emission points are labeled with alphanumeric codes. Codes with the same letter belong to the same field. Background images are extracted from the most recent high-resolution imagery in the ESRI, Google Satellite or Bing Aerial web portals.

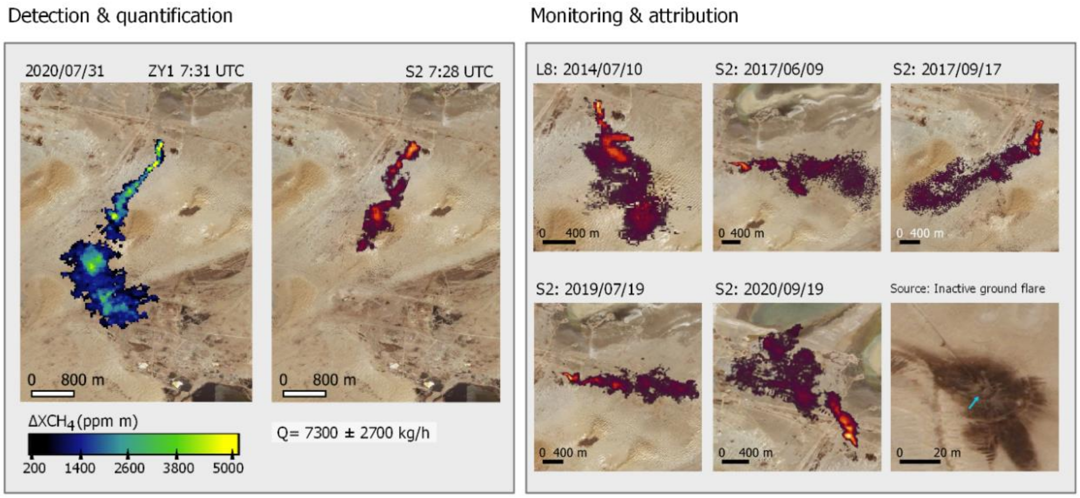

Figure 3. Examples of emissions detected from the A.3 emission point (see Fig. 2). Left, plume detected by both ZY1 and S2 within a 3-minute time difference. Right, time series of plumes detected at A.3 with the S2 and L8 multispectral satellites. A true-color composite of the emission point, based on visual imagery, is shown in the lower right corner. The background image for all panels is from Bing Aerial.

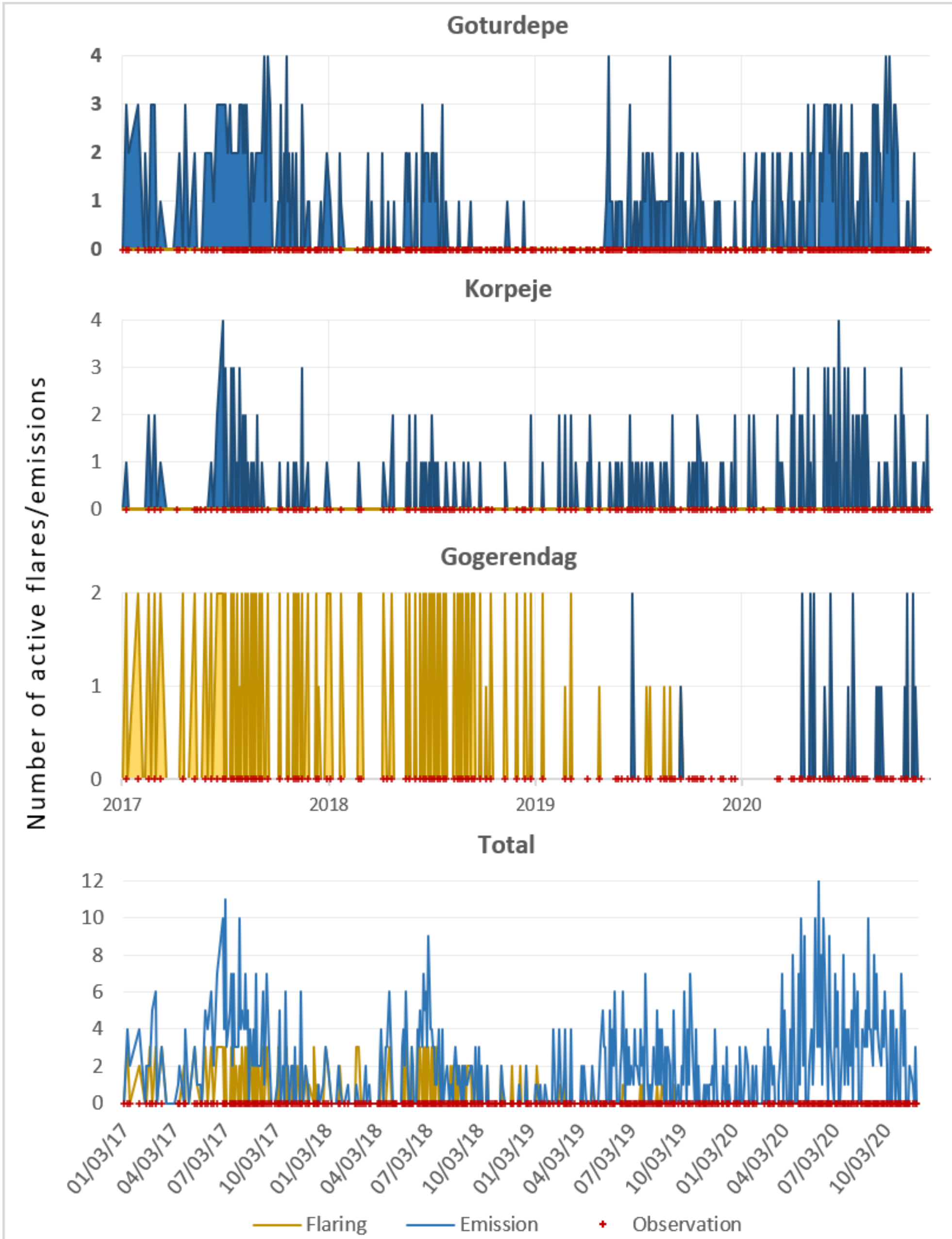

Figure 4. Temporal evolution of emissions in the Goturdepe (A.X), Korpeje (D.X) and Gogerendag (C.X) fields, as well as the daily total number of active emissions detected from the 29 sites found in this study. The vertical axis indicates the number of points that were emitting or flaring at the same time on the same day.

Table 1. Classification of oil and gas production fields where emissions have been found. "Field" refers to the name of the field; "Oil and Gas Category" is the type of production activity in each field; "Production" is the amount of production in kbbl/day in the years 2018-2020; "Number of emitters" is the number of emitting points that have been found in each field; "Detected emissions" is the number of days with emissions that have been observed by year; and "Total emissions" is the total number of plumes observed in each field in the entire study period. Oil and Gas category and production data is based on Rystad database (35).

Field	Oil and Gas Category	Production (kbbl/d)			Number of emitters	Detected emissions				Total emissions
		2018	2019	2020		2017	2018	2019	2020	
Goturdepe	Crude Oil	43.014	30.000	30.137	10	138	50	64	141	393
	Condensate	0.001	0.001	0.001						
	NGL	0.060	0.042	0.042						
Barsa-Gelmez	Crude Oil	28.000	20.000	13.667	4	32	39	23	32	126
	Condensate	0.001	0.001	0.059						
	NGL	0.021	0.015	0.029						
Gogerendag	Crude Oil	0.000	0.000	0.007	2	0	0	3	21	24
	Condensate	0.003	0.004	0.009						
Korpeje	Crude Oil	0.003	0.003	0.046	7	45	25	43	74	187
	Condensate	0.002	0.002	0.002						
	NGL	0.160	0.160	0.158						
	Gas	18.919	18.919	18.879						
Gamyshlja Gunorta	Crude Oil	0.004	0.003	0.768	2	7	14	24	28	73
	Condensate	0.003	0.003	0.683						
Keymir	Crude Oil	0.003	0.004	4.648	3	7	17	25	41	90
	Condensate	0.001	0.001	4.212						
	NGL	0.028	0.028	0.650						
Akpatlavuk	Crude Oil	0.004	0.003	0.000	1	21	16	12	2	51
	Condensate	0.003	0.003	0.000						
Total		90.23	69.19	74.00	28	250	161	194	339	944

Supplementary Information for

Satellites unveil easily-fixable super-emissions in one of the world's largest methane hotspot regions

Itziar Irakulis-Loitxate[1*], Luis Guanter[1], Joannes D. Maasakkers[2], Daniel Zavala-Araiza[3,4], Ilse Aben[2]

* Correspondence to: iiraloi@doctor.upv.es

This section includes:

Figures S1 to S9

Tables S1 to S1

SI References

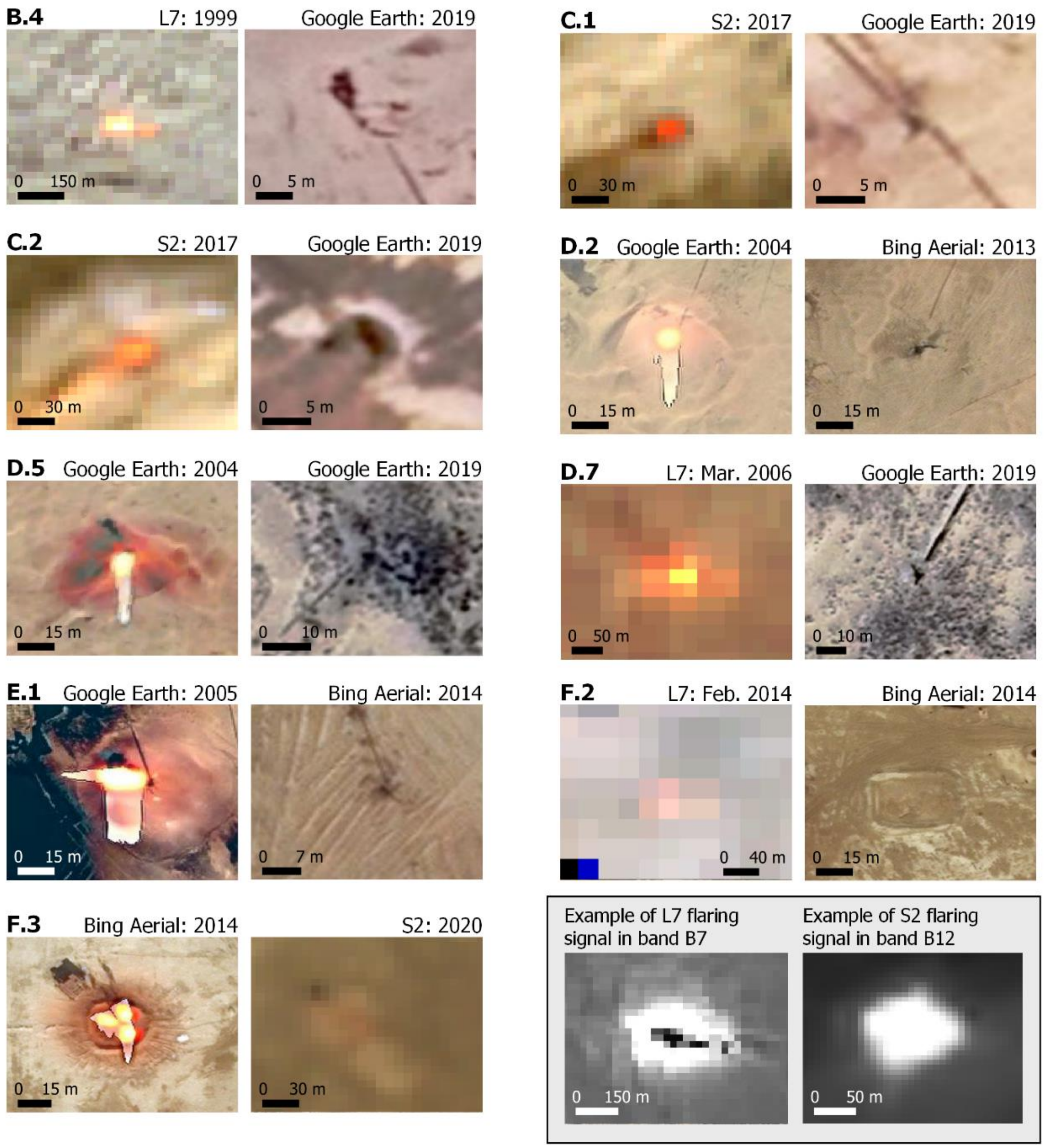

Fig. S1. Flares with active flaring in the past and current inactive appearance seen in RGB. Bottom right two examples of active flares as seen in the Landsat 7 (L7) B7 and S2 B12 bands (points D.7 and C.2 respectively), i.e. in the CH4 absorption bands. In the Landsat B7 and S2 B12 bands, the CH4 absorbs the signal (low values), while the flaring emits a very high signal (very high values) compared to the surface.

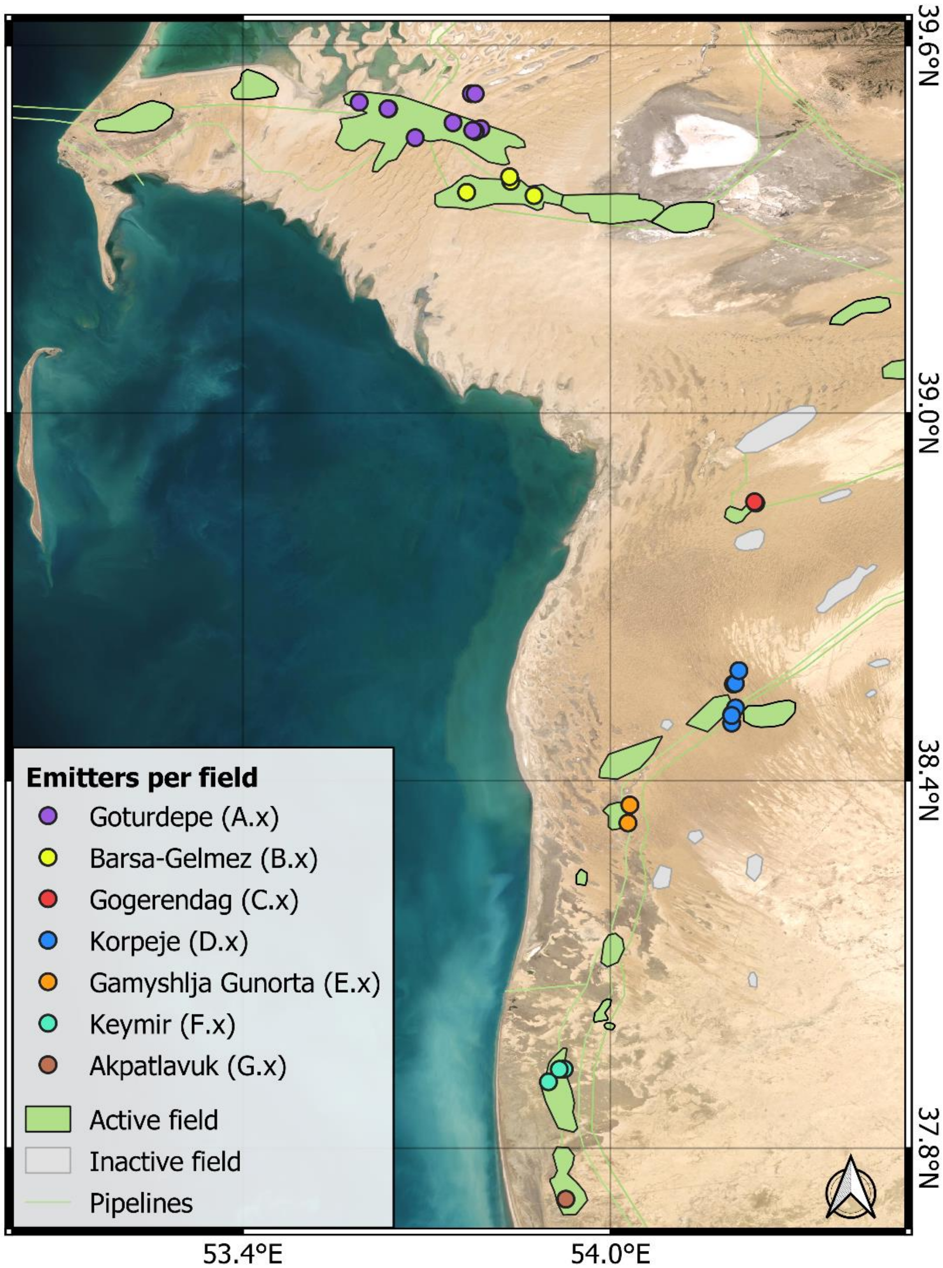

Fig. S2. Distribution of the detected points according to the field they belong to. The area of the fields is based on the data from Rose et al. 2018 (1). The extension of some fields has been manually updated due to their expansion in recent years.

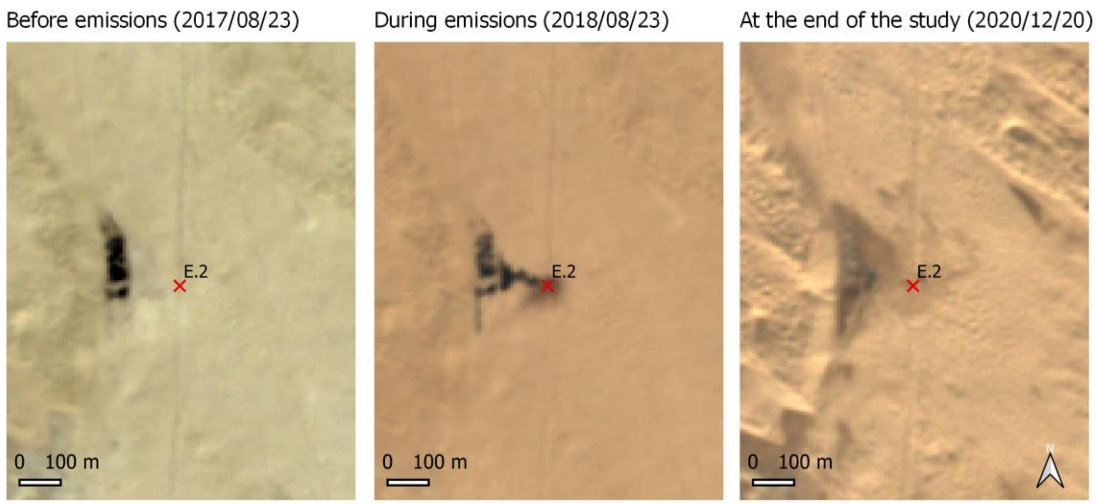

Fig. S3. The evolution of the E.2 emission point seen in RGB before, during and after the emissions derived from a leak. During the emission period a black liquid emanating from the emission point is visible.

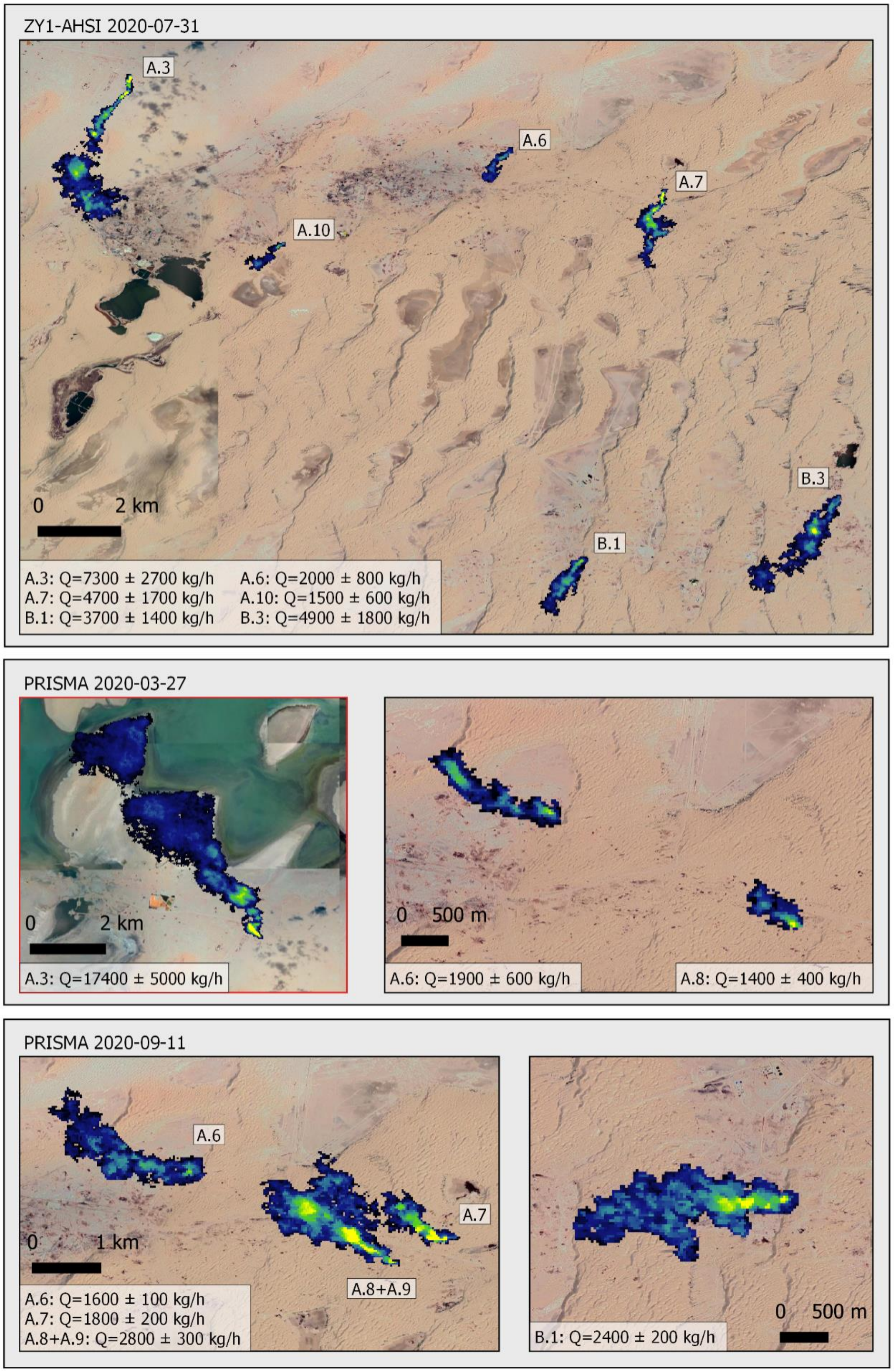
ZY1-AHSI 2020-07-31
A.3
A.6
A.7
A.10
B.3
B.1
0 2 km
A.3: Q=7300 ± 2700 kg/h
A.6: Q=2000 ± 800 kg/h
A.7: Q=4700 ± 1700 kg/h
A.10: Q=1500 ± 600 kg/h
B.1: Q=3700 ± 1400 kg/h
B.3: Q=4900 ± 1800 kg/h
PRISMA 2020-03-27
0 2 km
A.3: Q=17400 ± 5000 kg/h
0 500 m
A.6: Q=1900 ± 600 kg/h
A.8: Q=1400 ± 400 kg/h
PRISMA 2020-09-11
A.6
A.7
0 1 km
A.8+A.9
A.6: Q=1600 ± 100 kg/h
A.7: Q=1800 ± 200 kg/h
A.8+A.9: Q=2800 ± 300 kg/h
0 500 m
B.1: Q=2400 ± 200 kg/h

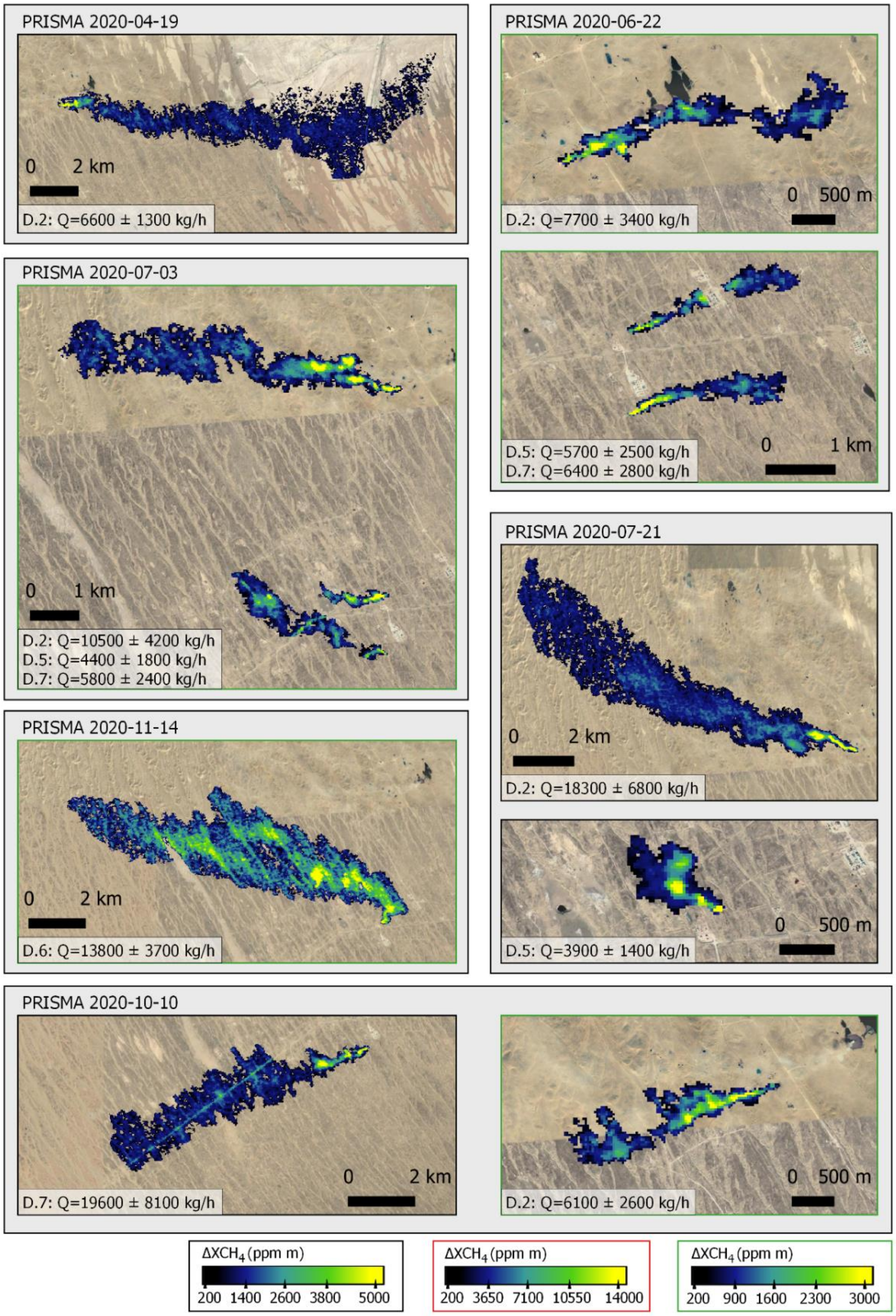

Fig. S4. All CH_4 plumes detected with the ZY1 and PRISMA hyperspectral satellites in the survey period. The color scale corresponding to each plume is indicated with the color of the map outline (black, red, or green).

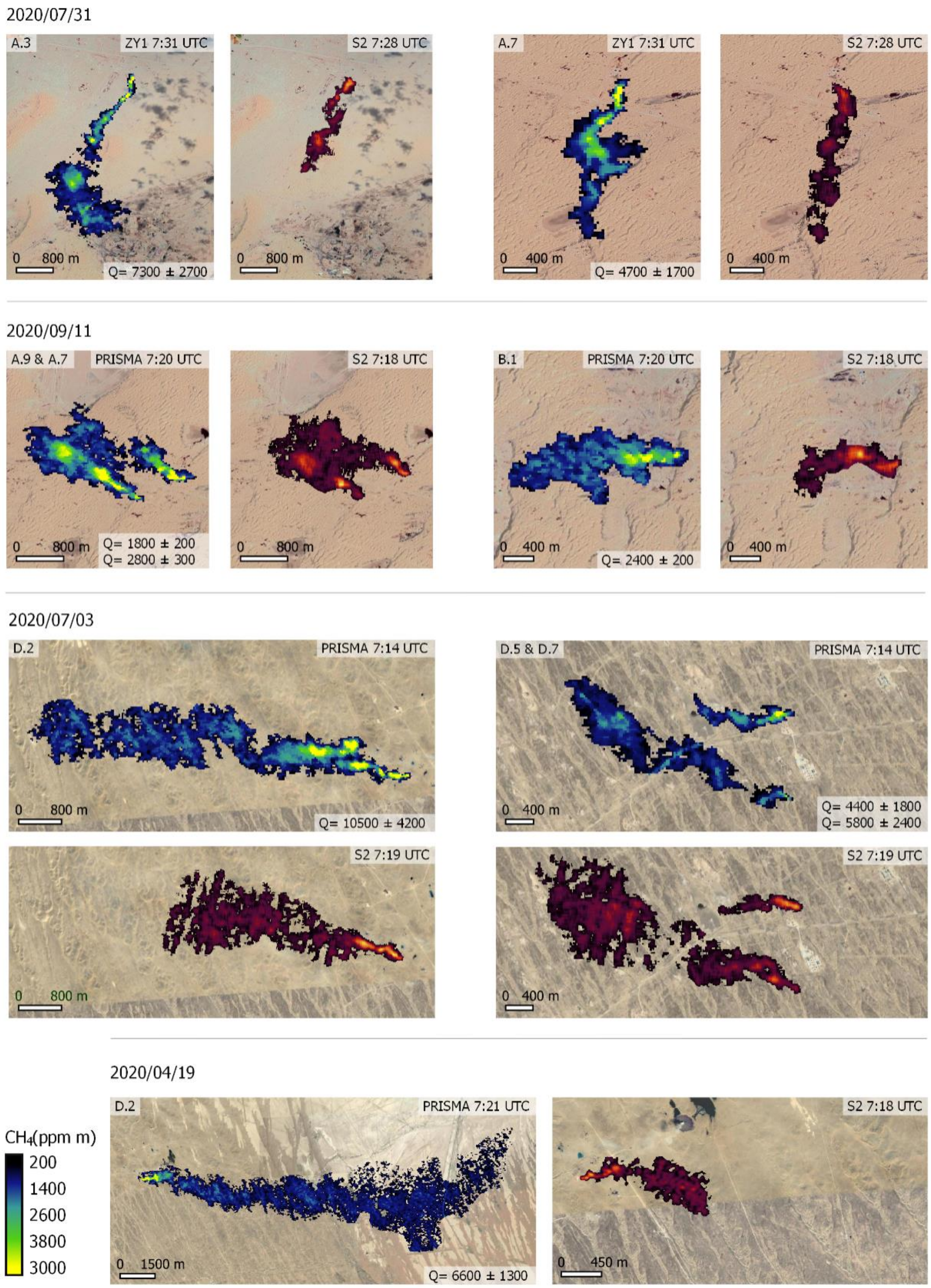

Fig. S5. Simultaneous detections of Sentinel 2 (S2) CH_4 plumes with PRISMA and ZY1 satellites within minutes of each other.

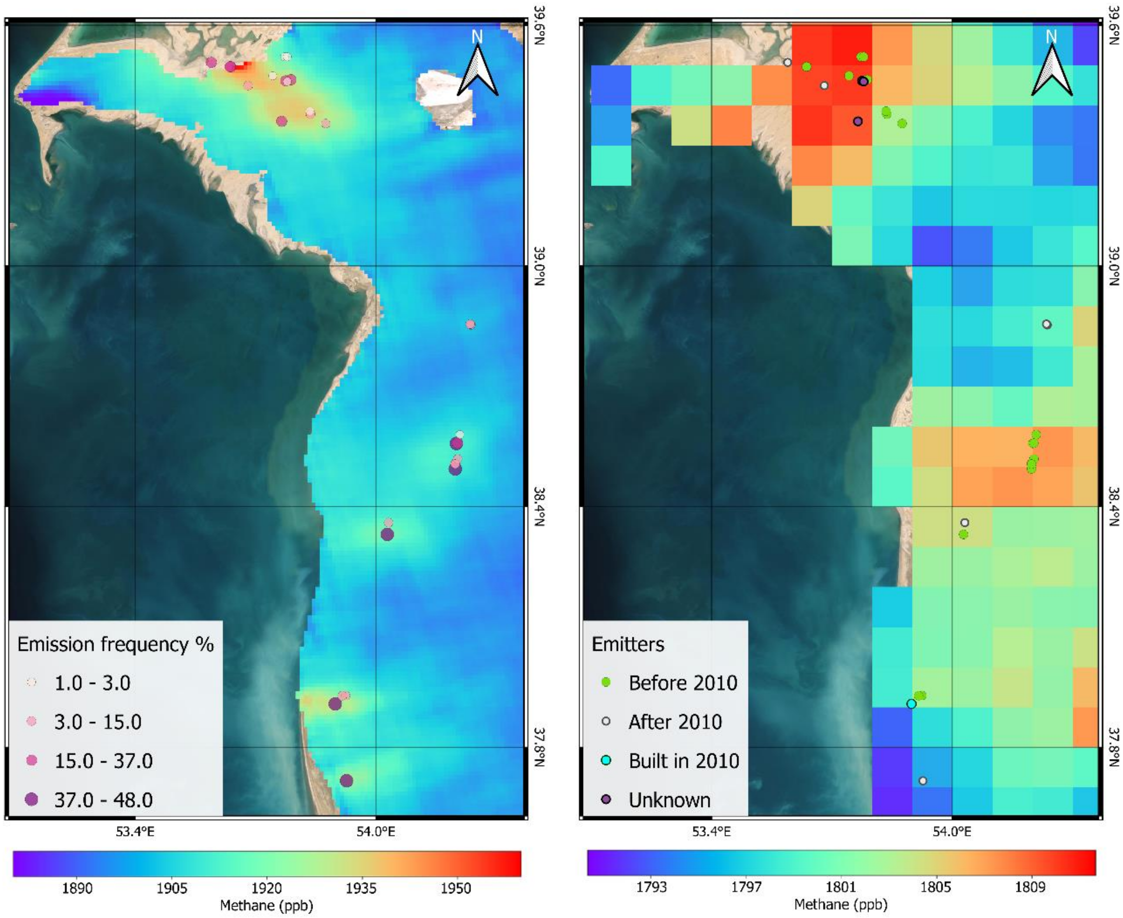

Fig. S6. Combination of moderate and low-resolution data from TROPOMI and SCIAMACHY sensors respectively with the emitter points indicated. On the left, the oversampled TROPOMI data between 2018 and 2020 combined with the emitters represented in terms of emission frequency. On the right the SCIAMACHY data oversampled to a 0.1º x 0.1º grid between 2003 and 2010 combined with the emitters found in this study classified according to their possible contribution to the SCIAMACHY data, i.e., whether the emitter existed before 2010 (it could have contributed to the CH4 enhancement), post-2010 (it could not have contributed), undefined (unidentified emitters) or if it was constructed just in 2010 (it existed in the SCIAMACHY observation period but its contribution should be minimal).

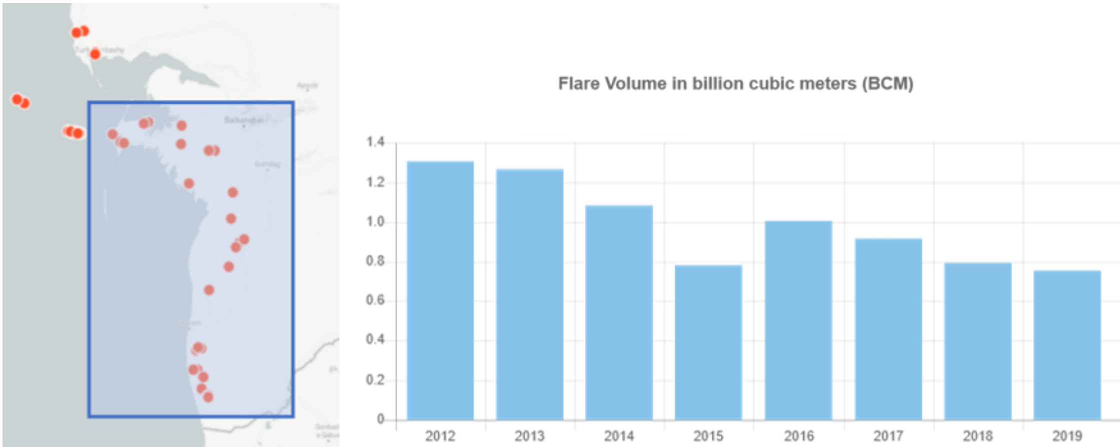

Fig. S7. VIIRS detected flaring over the years. On the left, inside the blue box, the onshore area of the South Caspian Basin that has been studied in this work, with the points where VIIRS detected flaring between 2012 and 2019. On the right the flared gas volume in that area according to VIIRS records each year (2). These data have been obtained from SkyTruth's Annual Flare Volume map (3).

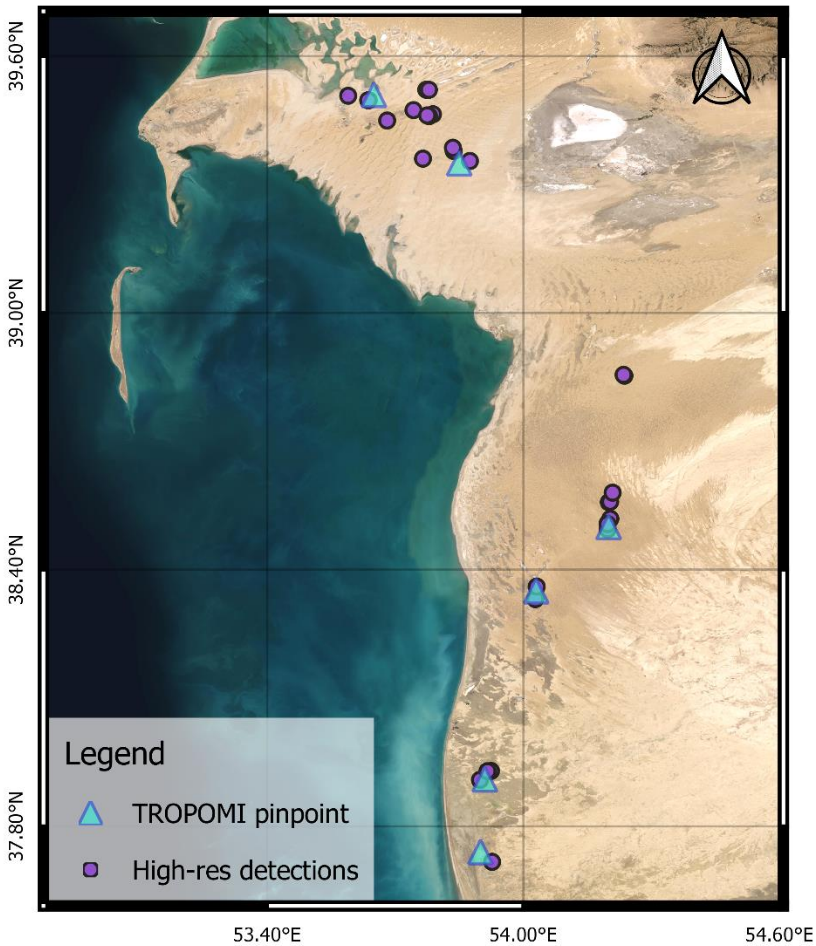

Fig. S8. The locations pinpointed by TROPOMI (blue triangles) and the emitter points (purple circles) found in the study.

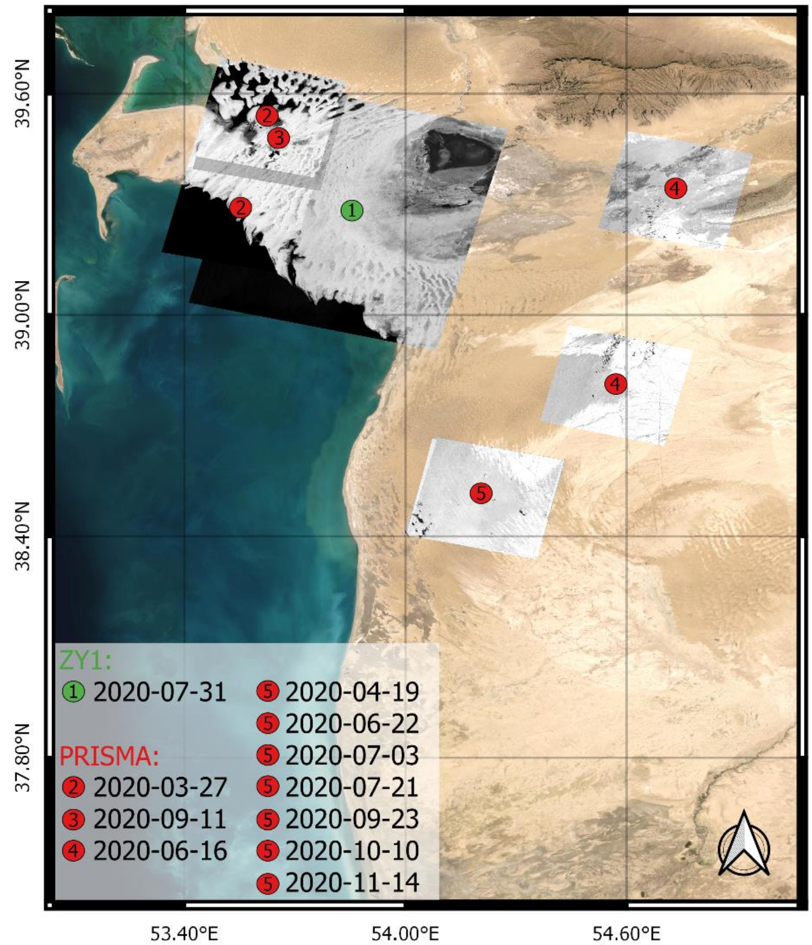

Fig. S9. Spatial coverage of ZY1 and PRISMA hyperspectral data used in this work.

Table S1. Emissions point list. Where "Point ID" is the identifying name assigned to this study. Lat and Long coordinates of the emitter. "Emitter" the type of emitter or source. "O. E. %" is Observed emission %, that is, the percentage of clear-sky days with emissions above the detection limit of S2, and this data is used throughout the document to refer to the emission frequency. "Field" field where it is located.

Point ID	Lat	Long	Emitter	O.E.%	Field
A.1	39.50741	53.58981	Ground flare	29	Goturdepe
A.2	39.49687	53.6367	Ground flare	20	Goturdepe
A.3	39.4968	53.63771	Ground flare	29	Goturdepe
A.4	39.52148	53.77274	Pit flare	1	Goturdepe
A.5	39.52137	53.77903	Ground flare	1	Goturdepe
A.6	39.4739	53.74292	Ground flare	1	Goturdepe
A.7	39.46428	53.78836	Pit flare	21	Goturdepe
A.8	39.4616	53.77502	Undefined	27	Goturdepe
A.9	39.45965	53.77921	Undefined	3	Goturdepe
A.10	39.44955	53.68117	Pipeline	9	Goturdepe
B.1	39.36045	53.76506	Undefined	18	Barsa-Gelmez
B.2	39.38584	53.83516	Ground flare	2	Barsa-Gelmez
B.3	39.37841	53.83704	Ground flare	14	Barsa-Gelmez
B.4	39.35498	53.87509	Ground flare	10	Barsa-Gelmez
C.1	38.85515	54.23498	Ground flare	7	Gogerendag
C.2	38.85308	54.23684	Ground flare	10	Gogerendag
D.1	38.57959	54.20931	Ground flare	1	Korpeje
D.2	38.55747	54.20049	Ground flare	41	Korpeje
D.3	38.55849	54.20353	Pit flare	26	Korpeje
D.4	38.51871	54.20393	Ground flare	7	Korpeje
D.5	38.50798	54.19769	Ground flare	8	Korpeje
D.6	38.50629	54.1976	Ground flare	7	Korpeje
D.7	38.49393	54.19764	Ground flare	39	Korpeje
E.1	38.33078	54.02832	Ground flare	42	Gamyshlja Gunorta
E.2	38.36017	54.03149	Pipeline	10	Gamyshlja Gunorta
F.1	37.90825	53.89857	Elevated flare	48	Keymir
F.2	37.9286	53.91623	Pit flare	12	Keymir
F.3	37.92913	53.92431	Pit flare	15	Keymir
G.1	37.71665	53.92702	Pit flare	38	Akpatlavuk

SI References

1. K. Rose, *et al.*, "Development of an Open Global Oil and Gas Infrastructure Inventory and Geodatabase" (2018) https:/doi.org/10.18141/1427573.

2. C. D. Elvidge, M. Zhizhin, K. Baugh, F. C. Hsu, T. Ghosh, Methods for global survey of natural gas flaring from visible infrared imaging radiometer suite data. *Energies* **9** (2016).

3. SkyTruth | Flaring Volume Estimates (March 5, 2021).